CrossMark
← click for updates

Synthesis of morphology-controlled bismutite for selective applications†

Thangavel Selvamani,[a] Balasubramaniam Gnana Sundara Raj,[a] Sambandam Anandan,*[a] Jerry J. Wu[b] and Muthupandian Ashokkumar*[c]

Bismutite ($Bi_2O_2CO_3$) possessing diverse morphologies, namely nanosheets, nanodiscs and nanoplatelets, was synthesized by a simple controllable method using bismuth nitrate pentahydrate and urea as precursors in a water/ethylene glycol mixture. The as-synthesized samples showed unique physical and chemical properties, such as varying morphology, phase identification, chemical composition, surface area and surface potential. $Bi_2O_2CO_3$ nanosheets exhibited excellent adsorption capabilities for anionic dyes (acid orange 7 and methyl orange) and high photocatalytic performance for the decolorization of cationic dyes (rhodamine B and methylene blue) under simulated solar illumination. Furthermore, the electrochemical performance of $Bi_2O_2CO_3$ nanosheets showed good capacitance properties and hence could be a potential candidate for electrode materials in energy related applications.

Introduction

In general adsorption and photocatalysis are used in wastewater treatment (environmental remediation) for the removal/degradation of inorganic (heavy metals), organic (dyes, drugs and herbicides), and biological pollutants (virus and bacteria).[1–5] Often, the selective adsorption of pollutants is a major issue and hence the development of better adsorbents is an active area of research.[6] Zhu *et al.* successfully developed the selective adsorption of cationic dyes using anionic metal–organic frameworks through guest–guest exchange between mixtures of aqueous dye solutions.[7] Ma *et al.* effectively prepared microporous anionic metal–organic frameworks for the selective adsorption of cationic dye from a mixture of organic dyes using the charge-selective separation ion exchange method.[8] Both cases comprised topologically controlled structures. Over the past few years, innovative synthesis of various materials for dye adsorption and selective photocatalysis has been reported.[5,9–22] The defects/oxygen vacancies play an important role in the

adsorption and photocatalytic behavior of these materials.[10,12,16,17,22] Alternatively, oxygen-rich compounds showed better adsorption and photocatalytic properties due to their unique physico-chemical properties.[18,21] Nevertheless, the photocatalytic activity of a photocatalyst depends upon band gap, surface area, surface potential and morphologies exposed facets.[23,24] Bismuth based oxides possess a narrow band gap, high charge carrier efficiency with good thermoelectric properties due to the overlap between 6s (Bi) and 2p (O) of a valance band.[25] Moreover, bismuth containing compounds have been used in many studies.[6,17–22,24–27] Among these $Bi_2O_2CO_3$ (bismutite) is an emerging material and used as an antibacterial, photocatalyst, sensor, supercapacitor, adsorbent and precursor for Bi_2O_3.[24,26,28–41] Bismutite belongs to Sillén phase compounds demonstrating inter-layer structures with alternative polymeric cationic $(BiO)_n^{n+}$ and anionic (CO_3^{2-}) layers and has been widely used as a photocatalyst for the degradation of toxic pollutants such as organic dyes and gaseous compounds such as nitric oxide (NO).[26,29–34,40–48] Greaves *et al.* first reported the synthesis of $Bi_2O_2CO_3$ through a simple chemical method and later, several methodologies have been reported for the synthesis of bismutite with various morphologies such as microflowers, microspheres (rose, plate, pinon-like, sponge-like, and hollow), persimmon-like, nanosheets, nanotubes, egg-tart and micro/nanostructures.[28–37,42–55] Chen *et al.* reported the synthesis of bismuth micro/nanospheres by a simple chemical method using ethylene glycol as a non-toxic solvent.[56] Numerous methods are available in the literature regarding the size and shape control of $Bi_2O_2CO_3$ *via* solvothermal, surfactant-assisted hydrothermal and vacuum heat treatments.[57–59] The concentration of precursors (citrate ion, nitrate ion, *etc.*), additives or precipitants (urea, sodium carbonate and ammonium

[a] *Nanomaterials and Solar Energy Conversion Lab, Department of Chemistry, National Institute of Technology, Tiruchirappalli-620 015, India.*
E-mail: sanand@nitt.edu; Fax: +91-431-2500133; Tel: +91-431-2503639
[b] *Department of Environmental Engineering and Science, Feng Chia University, Taichung 407, Taiwan*
[c] *School of Chemistry, University of Melbourne, Vic 3010, Australia.*
E-mail: masho@unimelb.edu.au; Fax: +61-3-93475180; Tel: +61-3-83447090

† Electronic supplementary information (ESI) available: (S1–S9) The FT-IR spectra of nanoplatelets and nanodiscs, the adsorption profile, XRD, FESEM and FT-IR spectra of $Bi_2O_2CO_3$ nanosheets before and after adsorption/photocatalytic processes, photographic images showing adsorption/photocatalytic processes for dye solutions. Tables (ST1–ST5) show unit cell parameters, calculated E_{VB}, E_{CB} from E_g values, RR(%), adsorption capacities and comparison of adsorption profiles. See DOI: 10.1039/c5cp07523h

7768 | *Phys. Chem. Chem. Phys.*, 2016, **18**, 7768–7779

This journal is © the Owner Societies 2016

carbonate, *etc.*) also plays a major role in achieving diverse morphologies of $Bi_2O_2CO_3$.[60–63] Likewise, the effect of co-solvent (water/ethanol or water/ethylene glycol) for various other materials has been extensively studied in order to attain excellent physico-chemical characteristics.[64–66] These interesting approaches have also been implemented to attain tunable properties like surface area, surface potentials, band alignment with functional morphologies.[65–69] Hence, researchers are interested to achieve multifunctional behavior with highly efficient and excellent selective applications through composition-structural engineering aspects. Until now, to the best of our knowledge, the synthesis of $Bi_2O_2CO_3$ with mixed solvent (water/ethylene glycol) has not been reported and also extensively studied for selective applications. Herein, we report on the synthesis and characterization of $Bi_2O_2CO_3$ with various morphologies through a simple and controllable method to explore their applications in dye adsorption and photocatalytic activity. In addition, the electrochemical performance of as-synthesized samples was tested to evaluate its suitability as a supercapacitor.

Experimental

Chemicals

All chemicals were of analytical grade and used without further purification. Bismuth(III) nitrate pentahydrate (ACS reagent, 98%), urea (AR grade, 99%), acid orange 7 (AO7: 85%), methyl orange (MO; 85%), methyl red (MR), rhodamine B (Rh B; 95%), methylene blue (MB) and sodium sulfate were purchased from Sigma-Aldrich. Vulcan XC-72 and polyvinylidenefluoride (PVDF) were purchased from Fluka. *N*-Methyl-2-pyrrolidene (NMP), ethylene glycol (≥99%) and nitric acid (ACS reagent) were purchased from Merck.

Synthesis of diverse bismutite nanostructures

About 6.29 g of bismuth(III) nitrate pentahydrate was dissolved in 43 mL of ethylene glycol which was then mixed with 33 mL of urea solution (6.05 mol dm^{-3}) in a 100 mL round bottom flask. The initial pH of the reaction mixture was 1.2, which was then adjusted to 0.9 using concentrated nitric acid (2.1 mL). Then, the reaction mixture was refluxed at 110 °C for 9 h under atmospheric pressure with constant stirring. After completion of the reaction, white bismutite nanosheet powder was collected and washed with distilled water several times and then dried at 80 °C for 4 h. The nanoplatelet morphology was obtained by following similar experimental conditions but without the addition of concentrated nitric acid, whereas the nanodisc morphology was obtained by refluxing at 80 °C for 9 h keeping other conditions similar.

Characterization

The surface morphology was observed using a field emission scanning electron microscope (FESEM model JEOL 7401F) and a transmission electron microscope (TEM model JEOL JEM 2010). Chemical composition and elemental analysis were carried out using energy dispersive X-ray spectroscopy (EDS, Oxford Inc.).

The phase identification and crystal structures of the samples were determined by powder X-ray diffraction (XRD) using a Rigaku D/max-2500 diffractometer with a Ni-filtered Cu Kα radiation source (40 kV, 30 mA, λ = 1.5406 Å). Fourier transform infrared (FTIR) spectra were recorded on a Nicolet iS50 infrared spectrophotometer using the KBr pellet technique. Micro-Raman spectra of the sample were recorded by backscattering configuration using an EnSpectr RS-532 Raman system. X-ray photoelectron spectroscopy (XPS) measurements were recorded on a Physical Electronics PHI 5600 spectrophotometer with mono-chromatic Al Kα (1486.6 eV) X-ray as the excitation source. The nitrogen gas adsorption–desorption measurements were performed using a Micromeritics ASAP2010 at liquid nitrogen temperature (77 K) and surface area was calculated using the Brunauer–Emmett–Teller (BET) equation. Surface charge (ζ-potential) of the samples was measured at different pH values using a zeta-check-zeta-potential analyzer (Microtrac) apparatus. UV-visible absorption spectra (diffuse reflectance mode; DRS) were recorded using an ultraviolet-visible (UV-vis) spectrophotometer (T90+, PG instruments, UK) with an integrating sphere using $BaSO_4$ as a standard. The photoluminescence (PL) spectra of the samples were performed using a Shimadzu (RF5301PC) spectrofluorometer at an excitation wavelength (370 nm) under ambient conditions. The photocurrent measurement was performed using an AUTOLAB12/FRA2 in a three-electrode system; as-synthesized samples were coated on FTO as a working electrode and platinum (Pt) the counter as well as reference electrode with polymer ion gel being used as a solid electrolyte under a xenon illumination source (150 W with standard 85 mW cm^{-2}).

Adsorption studies

Adsorption studies were performed by magnetically stirring the mixture at room temperature (natural pH). In a typical process, 25 mg of the samples was taken in a 125 ml borosilicate glass bottle which contained 100 mL of organic dye solution (1×10^{-4} mol L^{-1}: AO7 and MO; 5×10^{-5} mol L^{-1}: MR, Rh B and MB). The suspension was constantly stirred and at regular time intervals about 4 mL aliquots of reaction mixtures were removed and filtered using a PVDF syringe filter (0.45 μm) to estimate the amount adsorbed. The amount of adsorbed dyes was quantified using a UV-vis spectrophotometer (T90+, PG instruments, UK). The removal ratios (RR) of adsorption for dyes was calculated using the formula RR = $(C_0 - C)/C_0 \times 100\%$. Then, the adsorption capacity of each dyes on the samples was calculated using $Q_m = (C_0 - C) \times V/m$. Here, the Q_m is the adsorption capacity (mg g^{-1}), C_0 and C are the concentrations of the dye (mg L^{-1}) before and after adsorption, respectively, V is the volume of solution (L) and m the mass of the samples taken (g). Furthermore, the selective adsorption of anionic dye (AO7 and MO) from a mixture (AO7 in MB and MO in MB) was studied under similar concentrations with as-synthesized samples as adsorbents.

Photocatalytic activity

Photocatalytic experiments of the synthesized samples were carried out at natural pH under ambient atmospheric conditions

This journal is © the Owner Societies 2016

Phys. Chem. Chem. Phys., 2016, **18**, 7768–7779 | 7769

using a 150 W tungsten halogen lamp ($\lambda \geq$ 400 nm; the intensity of incident radiation was 80 600 $\pm$ 10 Lux measured using Extec, USA). The samples (50 mg of catalyst) were dispersed in a 125 mL borosilicate glass bottle which contained 100 mL of organic dye solution (5×10^{-5} mol L^{-1}: Rh B and MB). Prior to illumination, the suspension was magnetically stirred in the dark for 30 min to attain adsorption/desorption equilibrium. During irradiation, 4 mL of solution was collected at regular time intervals from the suspension mixtures and the catalyst was filtered using a PVDF syringe filter (0.45 μm). The photocatalytic activity of synthesized samples was calculated by measuring the remaining concentration of organic dye using a UV-vis spectrophotometer (T90+, PG instruments, UK).

Electrochemical measurements

The working electrode was fabricated as described below: about 75 wt% bismutite, 20 wt% Vulcan XC-72 carbon (conductive agent) and 5 wt% of PVDF (binder) were ground in a mortar, and then a few drops of NMP solution was added to form a slurry. The slurry was then coated onto a pretreated SS plate (active electrode area was 1.0 cm^2) and dried at 100 °C under vacuum for 12 h. Capacitance measurements were performed using a standard three-electrode system containing the above prepared SS plate as a working electrode, Pt foil as a counter electrode, and Ag/AgCl as a reference electrode in 1 M Na$_2$SO$_4$ aqueous solution as an electrolyte. Cyclic voltammetry (CV), galvanostatic (GV) charge–discharge and electrochemical impedance spectroscopy (EIS) techniques were performed at room temperature by using a potentiostat/galvanostat (AUTOLAB 302N module) as a testing system. The supercapacitor performance of the as-synthesized sample was measured at different scan rates (5, 10, 20, 40, 80 and 160 mV s^{-1}) within the potential range of −0.1 to +0.4 V. Then, a long term galvanostatic charge–discharge performance was carried out up to 1000 cycles at a current density of 0.1 mA cm^{-2} in the potential range of −0.1 to +0.4 V. The specific capacitance (SC) for as-prepared working electrodes was calculated from galvanostatic discharge curves using eqn (1).

$$SC = \frac{It}{m\Delta E} \qquad (1)$$

where, I is the current applied (amperes), t is the discharging time in seconds, m is the mass of the sample present on the electrode in grams and ΔE is the operating potential window in volts of charge and discharge. Furthermore, the electrochemical impedance spectroscopic measurements were carried out in the alternating current frequency range of 0.1 Hz–100 kHz at open circuit voltage with an excitation signal of 10 mV for an impedance spectrum analysis.

Results and discussion

Microscopic observations

Morphological features of the as-synthesized sample (refluxed at 110 °C for 9 h in the presence of concentrated nitric acid) are shown in Fig. 1a and b. The low magnification FESEM image
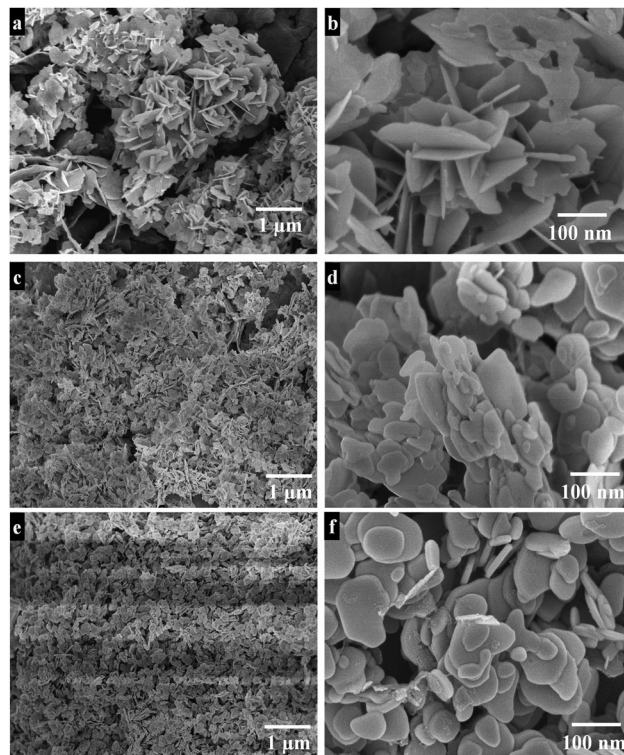

Fig. 1 Low and High magnification FESEM images of Bi$_2$O$_2$CO$_3$ nanosheets (a and b), nanoplatelets (c and d) and nanodiscs (e and f).

(Fig. 1a) shows that the as-synthesized sample has a sheet-like morphology. A high magnification image (Fig. 1b) shows that each sheet is about 200–300 nm in length and 5–10 nm in thickness. Platelet-like morphology (Fig. 1c and d) is seen for the preparation procedure in the absence of concentrated nitric acid, while under similar reaction conditions, upon refluxing at 80 °C for 9 h disc-like morphology with 50–100 nm diameter and 10–15 nm thickness is produced (Fig. 1e and f). TEM results of the synthesized sample (refluxed at 110 °C for 9 h in the presence of concentrated nitric acid) reveal nanosheet morphology with immensely porous architecture and lateral dimensions of 200–300 nm in length and 300–500 nm in width (Fig. 2a and b). The observed lattice fringe d space of 0.271 nm in HRTEM is in good agreement with the (110) plane of interplanar distance for nanosheets of bismutite (Fig. 2c). Furthermore, the selected area electron diffraction (SAED) patterns of nanosheets confirm that diffraction rings which are in good agreement with the polycrystalline nature of the tetragonal structure of bismutite (Fig. 2d). The EDS spectrum (Fig. 2e) of nanosheets shows the presence of Bi, C and O elements confirming that synthesized material is pure Bi$_2$O$_2$CO$_3$.

Spectroscopic data

Powder XRD patterns of as-synthesized samples are shown in Fig. 3. All diffraction lines can be indexed to the tetragonal phase of Bi$_2$O$_2$CO$_3$ which are in good agreement with analogous JCPDS card no. 41-1488. Here, the distinct diffraction patterns at (2θ) 30.2, 32.6 and 46.8 lines correspond to (013), (110) and (020)
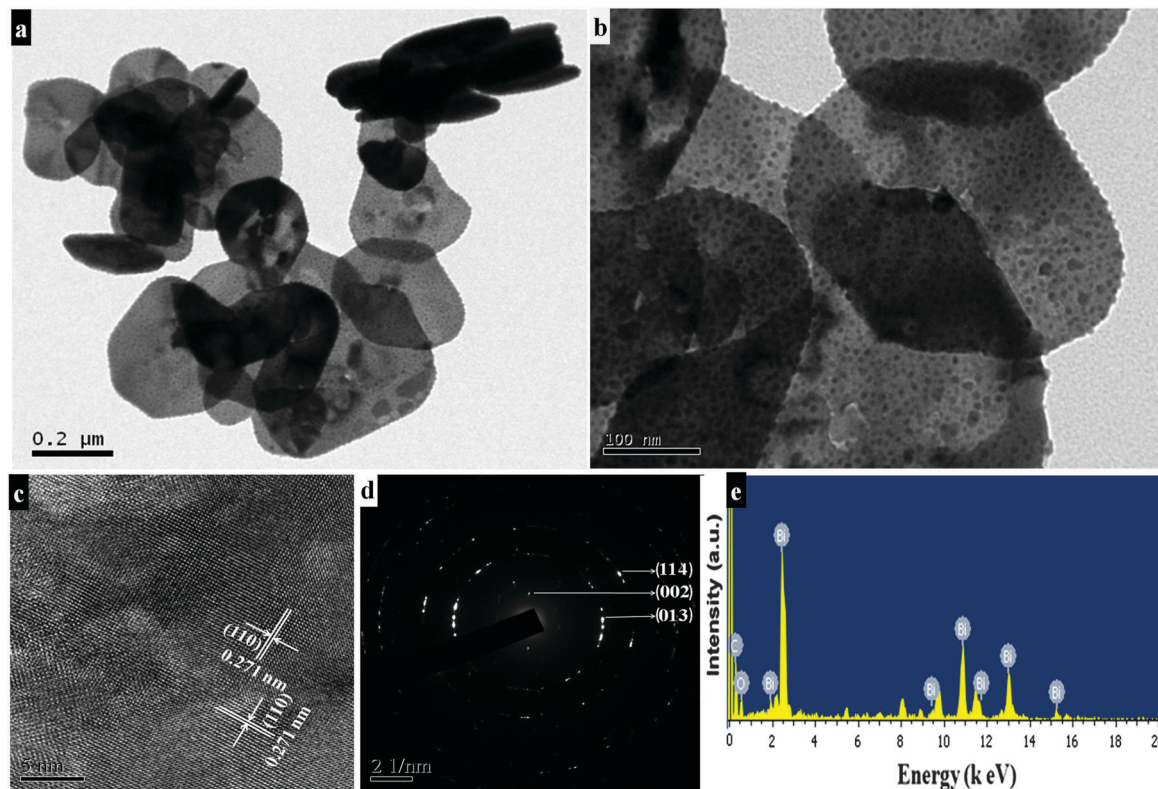
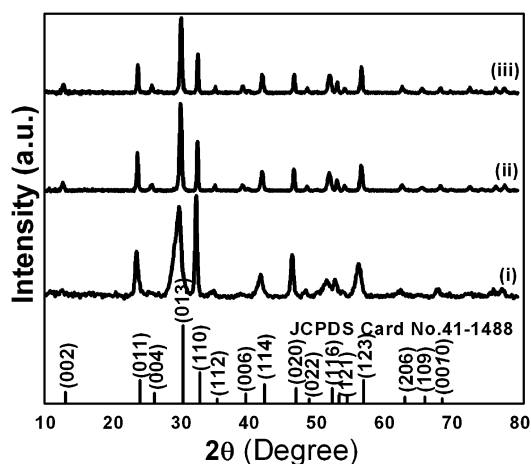Fig. 2   TEM images (a and b), HRTEM image (c), SAED pattern (d) and EDS spectrum (e) of $Bi_2O_2CO_3$ nanosheets.

Fig. 3   Powder XRD patterns of $Bi_2O_2CO_3$ nanosheets (i), nanoplatelets (ii) and nanodiscs (iii).

planes, respectively indicating the diverse nanostructures obtained during the reaction process. The intensity of diffraction lines attributes to the control over different growth orientations (crystallographic direction).[17] In addition, the line broadening at 30.2 (013 plane) for nanosheets indicates smaller crystallites when compared with other morphologies. While all other morphologies show high crystallinity with the pure tetragonal phase of bismutite. The crystal sizes of as-synthesized samples are found to be 24, 28 and 29 nm for nanosheets, nanodiscs and nanoplatelets, respectively, calculated using Debye–Scherrer's

formula for the most intense line at 30.2 (013 plane). The unit cell parameters of as-synthesized samples can be calculated using the least squares method and are given in Table ST1 (see ESI†). The FTIR spectrum of nanosheets is shown in Fig. 4a. The spectrum confirms the presence of carbonate ion (CO_3^{2-}) characteristic peaks which could be observed at 1036 cm^{-1} for symmetric vibration (ν_1), 1376 cm^{-1} and 1462 cm^{-1} (broad shoulder) for anti-symmetric vibration (ν_3), 838 cm^{-1} for outer-plane bending (ν_2) and a shoulder at 690 cm^{-1} for inner-plane deformation (ν_4).[30] Also, the additional vibration peak at 2424 cm^{-1} is attributed to the presence of carbonate ions.[43] Other peaks at 3424 cm^{-1} and 1760 cm^{-1} could be assigned to the presence of surface O–H stretching due to chemisorbed and/or physisorbed water molecules. No additional characteristic vibration peaks are observed under a typical synthetic process which confirms the purity of $Bi_2O_2CO_3$. Similarly, the FT-IR spectra of nanodisc and nanoplatelet morphologies clearly indicate the formation of highly pure $Bi_2O_2CO_3$ (Fig. S1, see ESI†). Typical Raman spectra of $Bi_2O_2CO_3$ nanosheets are shown in Fig. 4b in which the characteristic peaks of CO_3^{2-} ions are observed at 1360, 1070 and 670 cm^{-1}, which could be attributed to ν_3, ν_1 and ν_4 vibrations, respectively. The metal–oxygen (Bi=O) stretching vibration peak could be observed at 518 cm^{-1}. Characteristic peaks at 161, 362 and 426 cm^{-1} are also obtained due to external vibration modes for Raman analysis.[45,70] The crystal lattice of anions (CO_3^{2-}) is hidden under the general positions (C_1) for bismutite. Therefore, all vibrational modes become active for both FTIR and Raman analysis (degeneracies are removed).[70] The chemical state of the elements
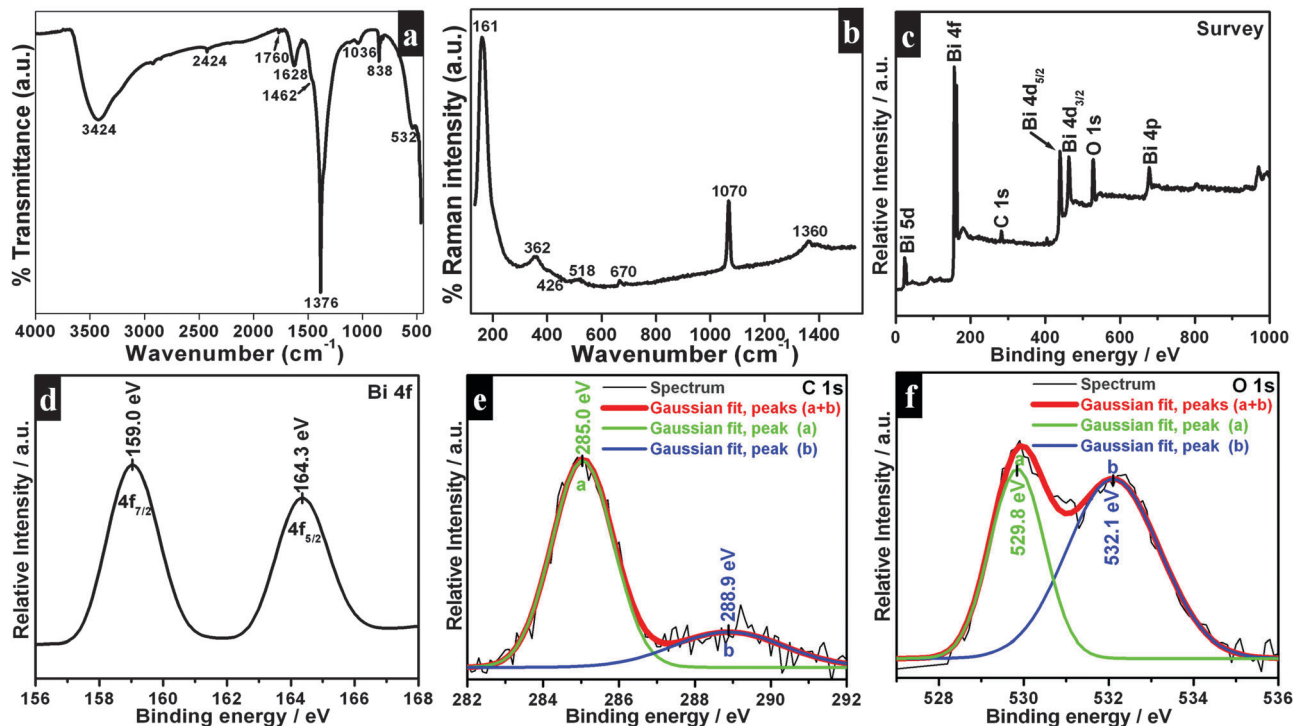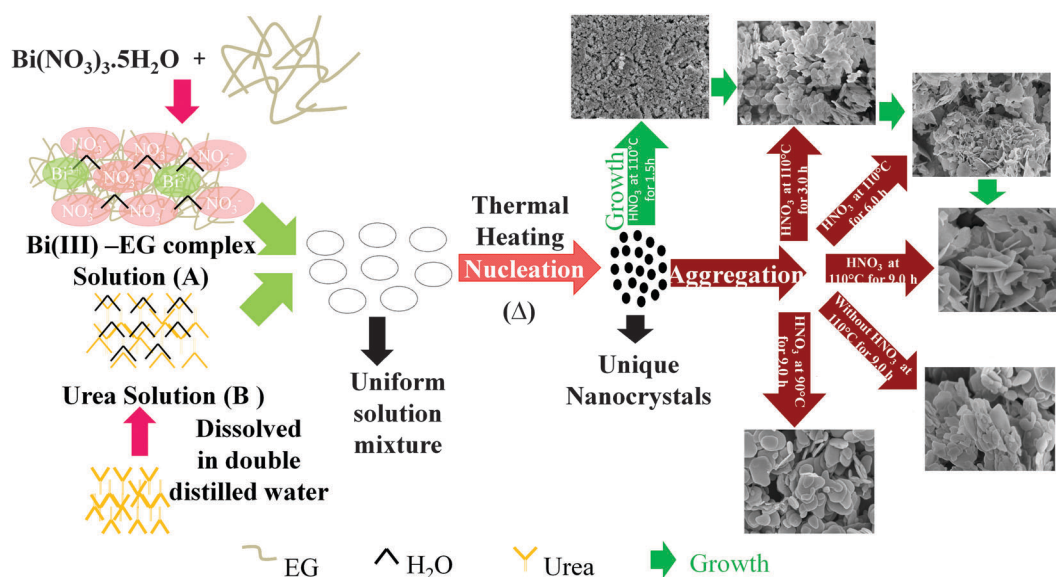
This journal is © the Owner Societies 2016

Phys. Chem. Chem. Phys., 2016, **18**, 7768–7779 | 7771

Fig. 4 FT–IR (a), Raman (b) and XPS spectrum (c–f) of $Bi_2O_2CO_3$ nanosheets.

and surface compositions of as-synthesized $Bi_2O_2CO_3$ nanosheets were confirmed by XPS (as shown in Fig. 4c–f). The survey spectrum (Fig. 4c) indicates the presence of Bi, C and O elements, which are located at 160, 288 and 530 eV for chemical binding energy states, respectively. Nevertheless, the core-level XPS signal of the Bi 4f element (Fig. 4d) displays two peaks at 159.0 and 164.3 eV for Bi $4f_{7/2}$ and Bi $4f_{5/2}$ which could be assigned for spin–orbit splitting of Bi^{3+} in the $Bi_2O_2CO_3$ sample. Although, C 1s spectra (Fig. 4e) obviously show two characteristic peaks at 285.0 and 288.9 eV which are due to carbonate ions (CO_3^{2-}) whereas the spectrum in

Fig. 4f demonstrates the O 1s state, confirmed by two peaks at 529.8 and 532.1 eV for Bi–O binding energy and carbonate ion species adsorbed with chemisorbed OH^- in the water molecule on to the surface of the sample, respectively.[31,45,46] Thus, the XPS spectrum also confirms that the as-synthesized sample is highly pure.

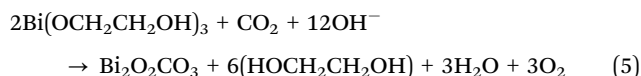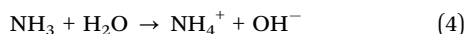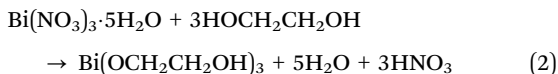### Mechanism for the formation of diverse nanostructures

A schematic illustration for the formation of bismutite with diverse morphologies is shown in Scheme 1. Reactions (2)–(5) show the formation of $Bi_2O_2CO_3$. $Bi(NO_3)_3\cdot5H_2O$ was dissolved

Scheme 1 Schematic illustration for the formation of diverse nanostructures of $Bi_2O_2CO_3$.

7772 | Phys. Chem. Chem. Phys., 2016, 18, 7768–7779

This journal is © the Owner Societies 2016

in ethylene glycol to produce glycolate complex solution (A) [reaction (2)].[71] Urea solution (B) was prepared by dissolving in double distilled water. When solutions (A) and (B) were mixed and heated to 110 °C, urea underwent hydrolysis to produces NH_4^+ and OH^- ions [reactions (3) and (4)]. During the course of reaction, the glycolate complex reacted with the product to generate unique nanocrystals of $Bi_2O_2CO_3$ [reaction (5)].

$$Bi(NO_3)_3 \cdot 5H_2O + 3HOCH_2CH_2OH$$
$$\rightarrow Bi(OCH_2CH_2OH)_3 + 5H_2O + 3HNO_3 \quad (2)$$

$$CO(NH_2)_2 + H_2O \rightarrow 2NH_3 + CO_2 \quad (3)$$

$$NH_3 + H_2O \rightarrow NH_4^+ + OH^- \quad (4)$$

$$2Bi(OCH_2CH_2OH)_3 + CO_2 + 12OH^-$$
$$\rightarrow Bi_2O_2CO_3 + 6(HOCH_2CH_2OH) + 3H_2O + 3O_2 \quad (5)$$

Here, ethylene glycol acts as a complexing agent as well as a co-solvent. However, the addition of concentrated nitric acid to the reaction mixture leads to the controlled complex formation between Bi(III) and EG due to the common ion effect (NO_3^-) which may affect the initial nucleation and growth to generate unique nanocrystals.[9] As a result, thinner $Bi_2O_2CO_3$ nanosheets are formed, whereas in the absence of concentrated nitric acid, intrinsic growth of nuclei leads to plate-like morphology. Experiments performed at lower temperature (80 °C) leads to the formation of only disc-like morphology due to the much slower rate of production of NH_4^+ and OH^- ions from urea hydrolysis. In order to understand the nanosheet growth process, experiments were performed at different time periods (1.5, 3 and 6 h) under identical conditions. The obtained samples were analyzed by both SEM and powder XRD (Fig. 5). In the case of the 1.5 h experiment, the obtained product is only nanocrystals of $Bi_2O_2CO_3$, whereas in the case of the 3 h experiment smaller nanocrystals aggregate into nanosheet-like morphology. In the case of the 6 h experiment nanosheet morphology is noticed due to Oswald ripping processes, whereas in the case of the 9 h experiment a well developed
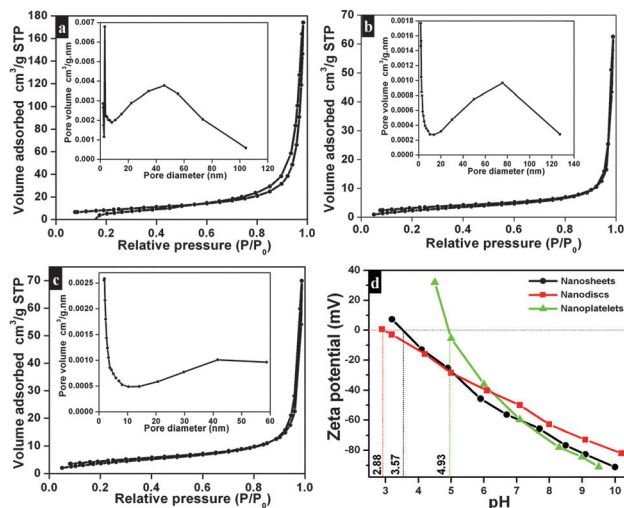

Fig. 6 Nitrogen gas adsorption/desorption isotherm of $Bi_2O_2CO_3$ nanosheets (a), nanoplatelets (b) and nanodiscs (c) (inset shows BHJ pore size distribution curves for the appropriate samples). The ζ-potential curve of $Bi_2O_2CO_3$ nanosheets, nanoplatelets and nanodiscs (d).

product, i.e., $Bi_2O_2CO_3$ nanosheets of 200–300 nm length and 5–10 nm thickness, is obtained. The powder XRD patterns also further support such nanosheet formation.

Surface area, pore size distributions and ζ-potential measurements

The nitrogen (N_2) adsorption–desorption isotherms and Barrett–Joyner–Halenda (BJH) pore size distribution of as-synthesized $Bi_2O_2CO_3$ nanosheets are shown in Fig. 6a. The adsorption isotherms resemble type-III which possess a macroporous surface with monolayer-multilayer adsorption. Also the adsorption hysteresis loops clearly indicate H3 type without any limiting adsorption at high P/P_0 values which may be due to the existence of plate-like particles or slit-like pores.[72,73] The calculated specific surface area of $Bi_2O_2CO_3$ nanosheets is about 30 m^2 g^{-1} calculated using the Brunauer–Emmett–Teller (BET) equation. The specific surface areas of $Bi_2O_2CO_3$ nanoplatelet and nanodisc morphologies are about 11 and 16 m^2 g^{-1}, respectively (Fig. 6b and c). The surface charges of as-synthesized $Bi_2O_2CO_3$ samples were determined by ζ-potential measurement: ζ-potential vs. pH is shown in Fig. 6d. It could be seen that it is positive at low pH and negative at high pH. The isoelectric point for all samples is below pH 7.

Adsorption of dyes

The adsorption capacities of as-synthesized $Bi_2O_2CO_3$ samples were evaluated by dispersing the samples in aqueous solutions containing dyes. AO7, MO, MR, Rh B and MB were chosen as model dye pollutants. Fig. 7a–e show UV-vis absorption spectra of above mentioned dyes. The percentage of the adsorption profile (RR) reveals that about 96% of AO7 adsorbed on $Bi_2O_2CO_3$ nanosheets in 60 min (Fig. 7a). The spectra shown in Fig. 7b indicate that the rate of adsorption of MO on $Bi_2O_2CO_3$ nanosheets is faster than that of AO7. However, only negligible amounts of neutral (MR) and cationic (Rh B and MB)
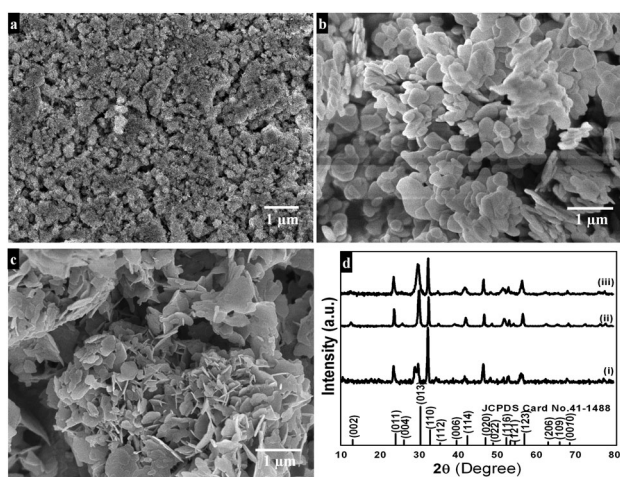

Fig. 5 FESEM images of $Bi_2O_2CO_3$ nanosheets at 1.5 h (a), 3.0 h (b) and 6.0 h (c). Powder XRD patterns of $Bi_2O_2CO_3$ nanosheets (d) at 1.5 h (i), 3.0 h (ii) and 6.0 h (iii).

This journal is © the Owner Societies 2016

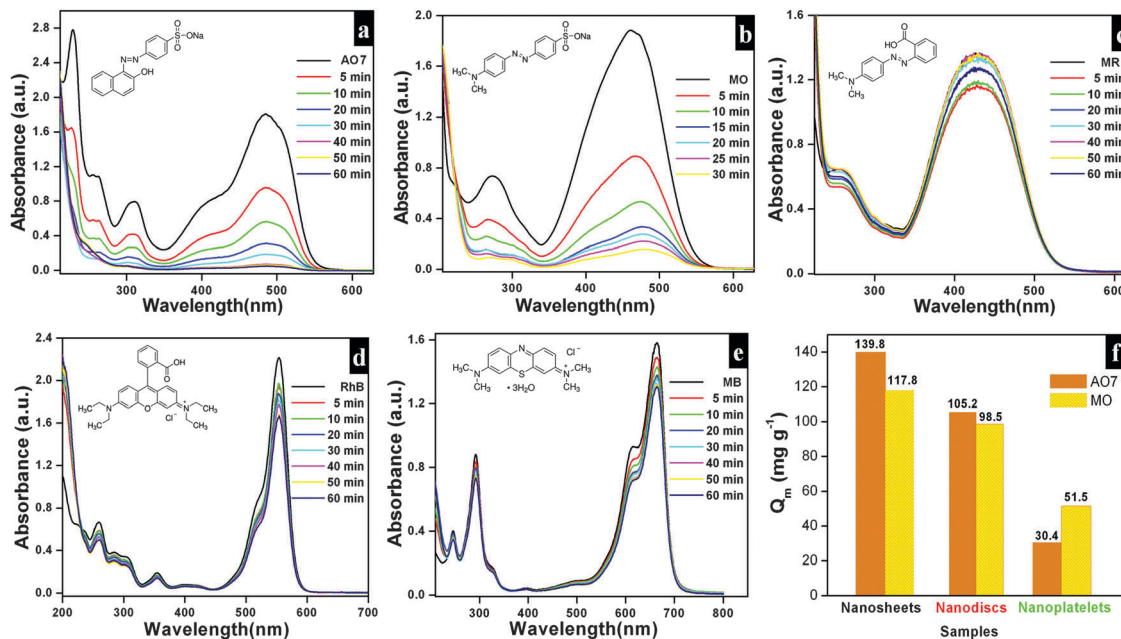Phys. Chem. Chem. Phys., 2016, 18, 7768–7779 | 7773

Fig. 7 Time dependence UV-vis absorption spectrum of Bi$_2$O$_2$CO$_3$ nanosheets in the presence of AO7 (a), MO (b), MR (c), Rh B (d) and MB (e) in the dark. The adsorption capacity profile for different morphologies of Bi$_2$O$_2$CO$_3$ in the presence of AO7 and MO (f).

dyes were adsorbed on as-synthesized Bi$_2$O$_2$CO$_3$ nanosheets (Fig. 7c–e). From the results, it could be suggested that Bi$_2$O$_2$CO$_3$ nanosheets exhibit selective adsorption towards anionic dyes only. Likewise experiments performed with the other morphologies (nanodiscs and nanoplatelets) show a percentage of the adsorption profile (RR) of about 75 and 21% towards AO7 and 78% and 40% for MO under identical conditions (Fig. S2, see ESI†). In addition, the adsorption capacities were calculated for as-synthesized samples and illustrated in Fig. 7f (statistical plot for AO7 and MO adsorption). Obviously, the nanosheets show enhanced adsorption capacity of AO7 about 139.8 mg g^{-1} which is significantly high compared with nanodiscs and nanoplatelets (105.2 mg g^{-1} and 30.4 mg g^{-1}, respectively). Likewise, MO shows higher adsorption on nanosheets (117.8 mg g^{-1}) compared to nanodiscs (98.5 mg g^{-1}) and nanoplatelets (51.5 mg g^{-1}). In order to explain the adsorption behavior of anionic, neutral and cationic dye molecules on as-synthesized Bi$_2$O$_2$CO$_3$ a possible mechanism is proposed and illustrated in Scheme 2.

The observed negative ζ-potential values (-58, -49 and -59 mV for nanosheets, nanodiscs and nanoplatelets) suggest that the prepared samples have OH groups adsorbed on the surface.[74,75] In the case of anionic dye, adsorption is caused by electrostatic stabilization/interaction between the adsorbent (as-synthesized Bi$_2$O$_2$CO$_3$ samples) and surface OH groups (negative ζ-potential), whilst in the case of neutral and cationic dyes there are no such electrostatic stabilization/interactions.[9,74] Molecular and microstructural level changes have taken place upon adsorption of anionic dye which could be confirmed by FESEM (undetermined morphology), FT-IR (characteristic band changes due to structural complexation) and powder XRD results (no changes in the tetragonal phase) (Fig. S3, see ESI†). Also experiments were carried out under identical conditions to
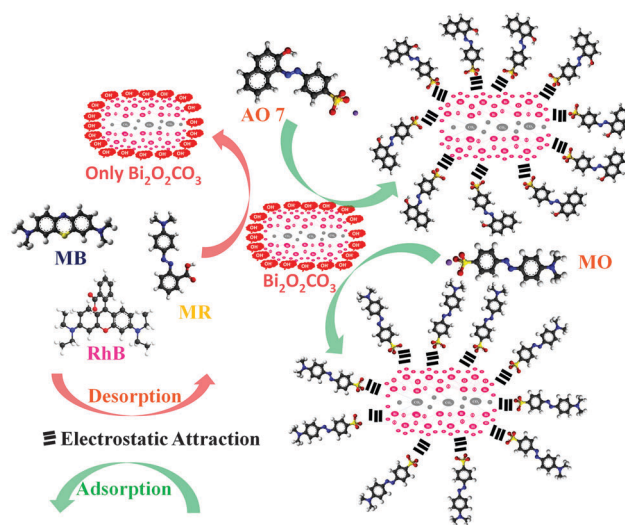
Scheme 2 Schematic representation of adsorption and desorption of dyes for as-synthesized Bi$_2$O$_2$CO$_3$ samples.

understand the preferential adsorption of certain dye in a dye mixture. In the case of AO7 and MB dye mixtures AO7 is selectively adsorbed (Fig. 8a) whereas MO and MB dyes adsorb due to co-adsorption caused by the inductive effect of dye molecules (Fig. 8b). Nevertheless, for AO7 and MB dye mixtures such an inductive effect caused by the MB molecule is prevented due to the steric hindrance of the AO7 structure (OH functional group is in the cis position towards –N=N– and the intra molecular hydrogen network) whereas in the MO molecular structure (the –N=N– azo group is in the trans position between two aromatic rings) no such steric hindrance is observed.[9]
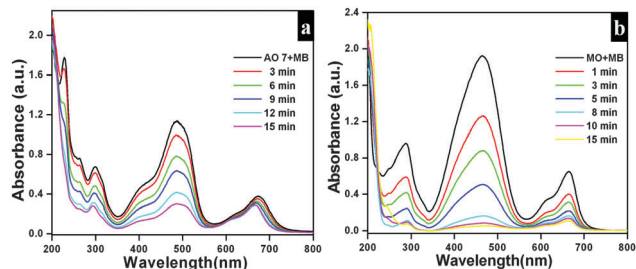
Fig. 8 (a) UV-vis absorption spectrum of $Bi_2O_2CO_3$ nanosheets in the presence of AO7 in MB (a) and MO in MB (b).

Photocatalytic activity and optical properties

The photocatalytic efficiencies of as-synthesized samples were evaluated using Rh B and MB (cationic dyes) as model pollutants. Fig. 9a shows the absorption spectra observed for Rh B solution during photocatalytic degradation in the presence of $Bi_2O_2CO_3$ nanosheets as a photocatalyst. Upon irradiation for 240 min, the characteristic absorption peak at 553 nm for Rh B gradually decreased. The photocatalytic degradation efficiency (D) for Rh B was calculated using eqn (6).

$$D = (A/A_0) \times 100 \qquad (6)$$

where A and A_0 are Rh B concentrations after and before degradation, respectively. For comparison, similar experiments were performed with $Bi_2O_2CO_3$ nanodiscs and nanoplatelets and as well as without any catalyst (blank test) and the results are shown in Fig. 9b. $Bi_2O_2CO_3$ nanosheets showed 98% decolorization of Rh B after 240 min under simulated solar illumination, while in the absence of a photocatalyst (blank test) only 3%

decolorization was observed (Fig. 9b). For $Bi_2O_2CO_3$ nanodisc and nanoplatelet morphologies about 80 and 70% decolorization of Rh B were observed under identical conditions. The higher photocatalytic activity for Rh B decolorization under $Bi_2O_2CO_3$ nanosheets could be attributed to its high surface area (30 m^2 g^{-1}), morphology and distinct textural properties (negative ζ-potential value).[23,43] Similarly, the photocatalytic degradation of other cationic dye (MB) was performed under identical conditions using as-synthesized $Bi_2O_2CO_3$ samples as the photocatalyst (Fig. S4, see ESI†). $Bi_2O_2CO_3$ nanosheets showed 95% decolorization of MB after 600 min under illumination whereas 48 and 66% were observed in the case of nanoplatelets and nanodiscs, respectively (Fig. S4, see ESI†). However, the photocatalysts do not show similar catalytic activity due to their molecular structure (Rh B has both partially positive and negative ions whereas MB has only positive ions).[9,76] In addition, possible adsorption/desorption of the dye molecules with specific textural characteristics of $Bi_2O_2CO_3$ samples influences the photocatalytic process.[75] Furthermore, the effect of photocatalytic activity was explained by facilitated optical absorption/emission characteristics (band gap/holes and electrons). The light absorption performance of $Bi_2O_2CO_3$ samples is shown in Fig. 9c. In addition absorption coefficients of as-synthesized samples were examined by Tauc plots. The optical absorption band gap of the semiconductor was calculated using eqn (7).[77]

$$\alpha = \frac{C \left(h\nu - E_g^{\text{bulk}} \right)^{1/2}}{h\nu} \qquad (7)$$

where α is the absorption coefficient, C is a constant, $h\nu$ is the photon energy and E_g^{bulk} is the band gap. The estimated band
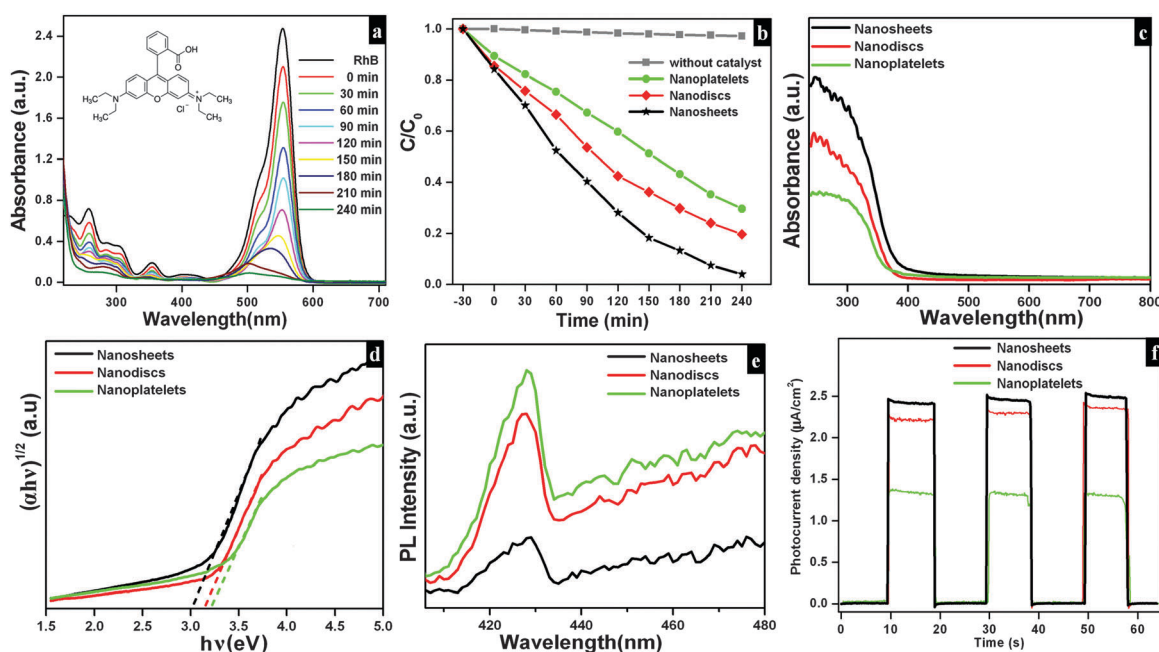

Fig. 9 Time dependence UV-vis absorption spectrum of $Bi_2O_2CO_3$ nanosheets in the presence of Rh B (a) under illumination. The photocatalytic degradation curve for different morphologies of $Bi_2O_2CO_3$ in the presence of Rh B (b). DRS absorption spectrum (c), corresponding Tauc plot (d), PL emission (e) and photocurrent responses (f) of $Bi_2O_2CO_3$ samples.
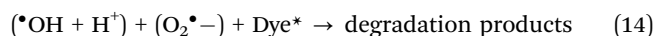
This journal is © the Owner Societies 2016

Phys. Chem. Chem. Phys., 2016, **18**, 7768–7779 | 7775
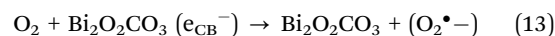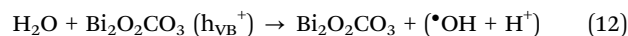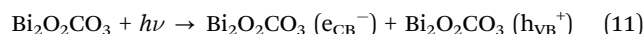
gaps of as-synthesized $Bi_2O_2CO_3$ samples are 3.02, 3.12 and 3.21 eV for nanosheets, nanodiscs and nanoplatelets, respectively, by the extrapolation of the linear region of $(\alpha h\nu)^{1/2}$ versus photon energy $h\nu$ plots (Fig. 9d).[77] The emission spectra of as-synthesized $Bi_2O_2CO_3$ show a strong emission peak at 428 nm (λ_{ex} = 370 nm), which could be attributed to photo-generated holes and electrons on the surface (Fig. 9e).[78] The emission intensity of $Bi_2O_2CO_3$ nanosheets is less intense due to the reduction in the recombination rate and separation of photogenerated carriers leading to a higher photocatalytic activity.[22] To support this, photocurrent density measurements were performed for as-synthesized $Bi_2O_2CO_3$ samples and are shown in Fig. 9f. $Bi_2O_2CO_3$ nanosheets obviously showed a much higher photocurrent response, which implies superior photocatalytic activity than that of nanodiscs and nanoplatelets (Fig. 9f). Based on the results of these studies for photocatalytic activity, a mechanism is suggested in Scheme 3. Here, the valance band (VB) and conduction band (CB) potentials of as-synthesized $Bi_2O_2CO_3$ samples can be calculated (Table ST2 (see ESI†)) using the following eqn (8)–(9)

$$E_{VB} = X - E_e + 0.5E_g \tag{8}$$

$$E_{CB} = E_{VB} - E_g \tag{9}$$

where X is the absolute electronegativity of $Bi_2O_2CO_3$, which is defined as the geometric average of the absolute electronegativities of the constituent atoms. E_e is the energy of free electrons on the hydrogen scale (E_e = 4.5 eV). X was found to be 6.543 eV for $Bi_2O_2CO_3$. However, the positioned CB value at 0.438 to 0.533 eV of as-synthesized $Bi_2O_2CO_3$ samples given in Table ST2 (ESI†) is more positive than that of $O_2/O_2^{\bullet-}$ (-0.28 eV vs. NHE) which implies that

photoreduction through the electron and the position of $^{\bullet}OH/H_2O$ (+2.27 eV vs. NHE) displays more positive than that of the VB suggesting photooxidation through holes, respectively. Meanwhile, the dye molecules are stable under simulated solar illumination (without a catalyst) and in the presence of a photocatalyst (dark condition). Under illumination, the dye is excited and leading to electron injection from the excited state of the dye into the CB of the photocatalyst (self-sensitization degradation).[79] In general, such photosensitization of photocatalysts is limited and follows the reactions proposed for photocatalytic degradation (reactions (10)–(14)).[80]

$$Dye + h\nu \rightarrow Dye^* \tag{10}$$

$$Bi_2O_2CO_3 + h\nu \rightarrow Bi_2O_2CO_3\ (e_{CB}^-) + Bi_2O_2CO_3\ (h_{VB}^+) \tag{11}$$

$$H_2O + Bi_2O_2CO_3\ (h_{VB}^+) \rightarrow Bi_2O_2CO_3 + (^{\bullet}OH + H^+) \tag{12}$$

$$O_2 + Bi_2O_2CO_3\ (e_{CB}^-) \rightarrow Bi_2O_2CO_3 + (O_2^{\bullet}-) \tag{13}$$

$$(^{\bullet}OH + H^+) + (O_2^{\bullet}-) + Dye^* \rightarrow \text{degradation products} \tag{14}$$

The results of as-synthesized $Bi_2O_2CO_3$ samples indicated that E_{CB} has more positive potential than that of Rh B dye (CB: -1.42 eV) and the highest light absorption wavelength at 553 nm in the visible region possesses photo-generated electrons from the excited Rh B (dye*) which leads to higher photocatalytic activity.[81] Although the favorable light absorption of Rh B and the amount of carboxylic groups (–COOH) leading to the interaction with the surface site of the photocatalyst are much more when compared with MB (unavailable functional group), whereas, in the case of MB with the CB (-3.60 eV vs. vacuum) with light absorption
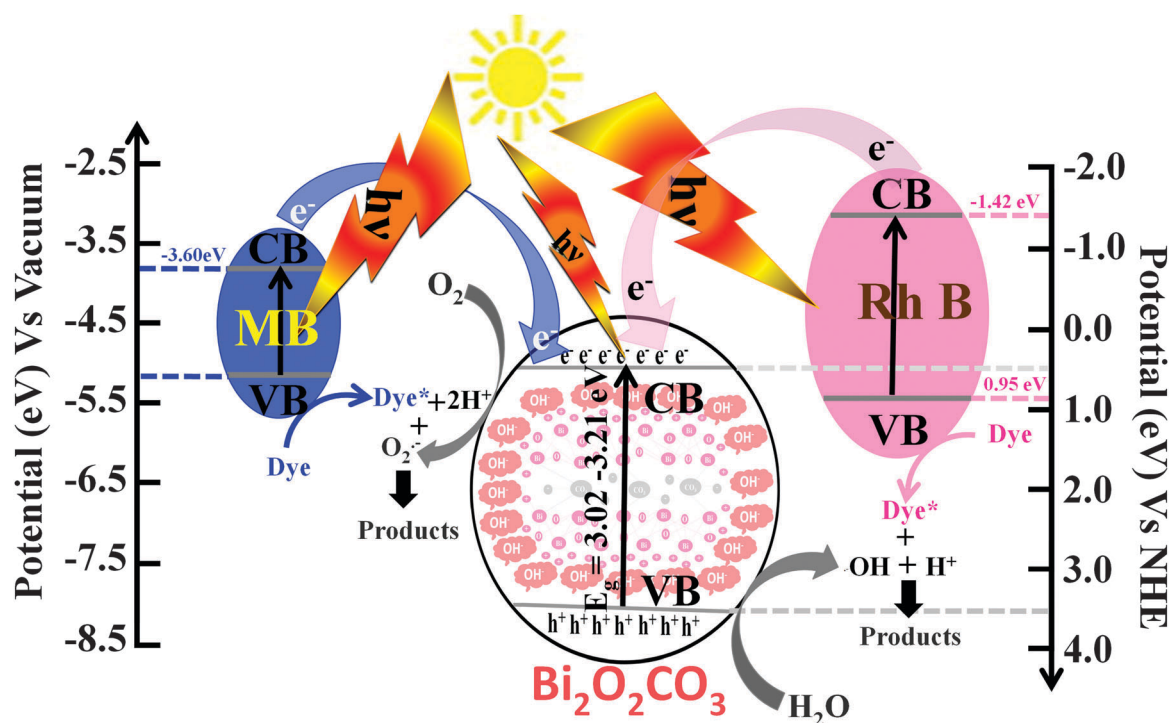
Scheme 3 Schematic demonstration showing the band structure and mechanism for the photocatalytic performances of dyes over as-synthesized $Bi_2O_2CO_3$ samples under simulated solar illumination.

at 664 nm apparently slower inclusion (week self-sensitization) for photo-generated electrons from the excited state and poor interaction with a photocatalyst surface site lead to lower photocatalytic activity. Therefore, as-synthesized $Bi_2O_2CO_3$ samples might have higher photocatalytic activity for Rh B than MB caused by the self-sensitization degradation process upon simulated solar illumination. In addition, the photocatalytic effect for the dye degradation process indeed influenced their physical parameters such as band gap, surface area, surface potential and morphology of as-synthesized samples.[23] Then, the materials' sustainability and reusability were studied after photodegradation by powder XRD, FESEM and FTIR analysis and the results are shown in Fig. S5 (see ESI†).

Electrochemical capacitance measurements

Electrochemical performances of as-synthesized $Bi_2O_2CO_3$ samples as electrode materials for a supercapacitor system were examined by cyclic voltammetry. Typical cyclic voltammogramms (Fig. 10a) are measured at a scan rate of 40 mV s^{-1} with potential ranging from −0.1 to 0.4 V *vs.* Ag/AgCl in a 1 M Na_2SO_4 aqueous electrolyte exhibiting ideal capacitive characteristics (without any redox peak currents in curves). Here, $Bi_2O_2CO_3$ nanosheet electrodes show greater integrated area and very high capacitance compared to nanodiscs and nanoplatelets. At different scan rates (5, 10, 20, 40, 80 and 160 mV s^{-1}) (Fig. 10b), the current response of electrode materials looks rectangular in shape with respect to the zero-current line and in addition peak current gets increased with increasing scan rates which illustrates the high capacitance (at low scan rate) and fast diffusion of ions (at a high scan rate).[82–84]

Hence, the specific capacitance of $Bi_2O_2CO_3$ nanosheet electrodes decreases much low when scan rates increased as shown in Fig. 10c. Furthermore, the GV charge–discharge behaviour of $Bi_2O_2CO_3$ nanosheet electrodes was examined using chronopotentiometry (CP) (potential ranges between −0.1 and 0.4 V *vs.* Ag/AgCl in a 1 M Na_2SO_4 aqueous electrolyte and current density 0.1 mA cm^{-2}). The charging and discharging profiles of $Bi_2O_2CO_3$ nanosheet electrodes are shown in linear variation (potential *vs.* time plot) which indicates that such material has high capacitance (Fig. 10d). The calculated specific capacitance value (83.5 F g^{-1}) for $Bi_2O_2CO_3$ nanosheet electrodes increases at higher cycles with the electrode surface being activated during the charging/discharging process.[85] Furthermore, the mechanistic characteristics of EIS for as-synthesized $Bi_2O_2CO_3$ samples were monitored. Fig. 10f shows the Nyquist impedance plots of as-synthesized samples exhibiting a semicircle over the high frequencies and a vertical line in the low frequencies. The semicircle at a high frequency range corresponds to the Faradaic charge transfer resistance (R_{ct}), which is mainly influenced by ionic resistances of the electrolyte and electrode active material interface. The vertical line at the low frequency range corresponds to ion diffusion of active electrode materials with respect to diffusive resistance at the electrolyte.[85,86] Herein, $Bi_2O_2CO_3$ nanosheet electrodes exhibiting a smaller semicircle at the high frequency region indicate that charge transfer resistance decreased extremely when compared with other electrodes such as nanodiscs and nanoplatelets. Hence, as-synthesized $Bi_2O_2CO_3$ nanosheet electrodes showing excellent specific capacitance and good cycling stability with highly
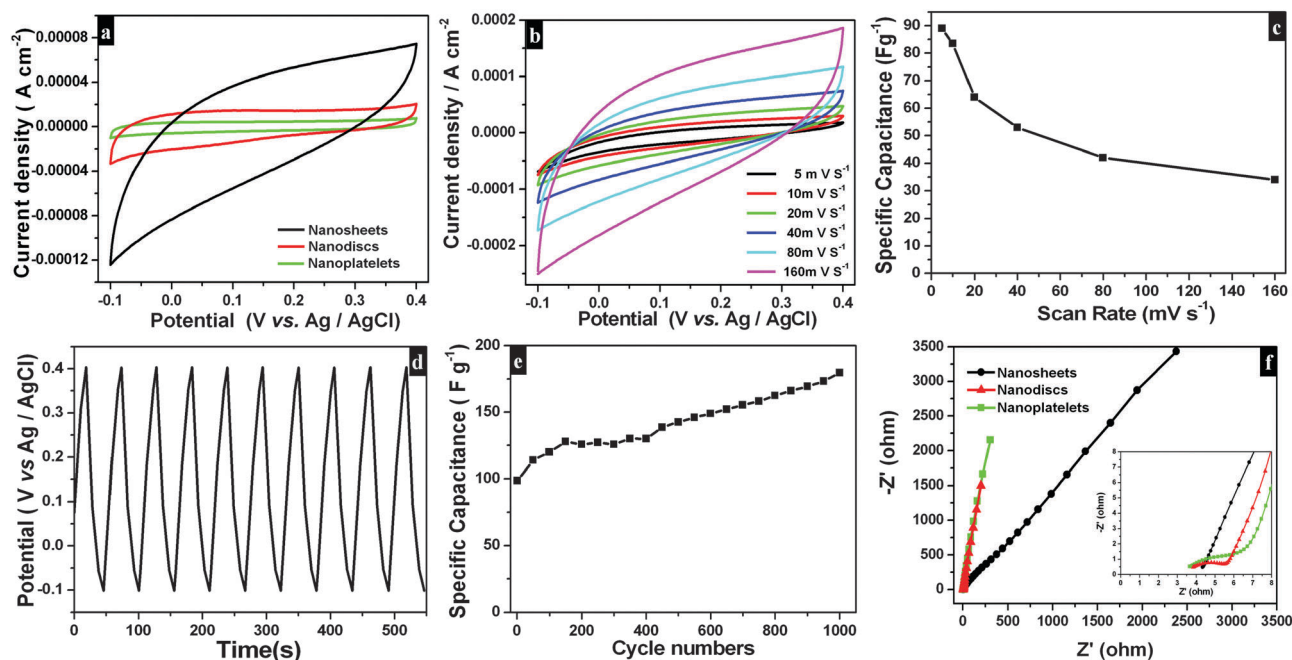
Fig. 10 CV curves (a) for different morphologies of $Bi_2O_2CO_3$ at 40 mV s^{-1} scan rate in 1 M Na_2SO_4 as an electrolyte. CV curves (b) and its corresponding specific capacitance plot (c) for $Bi_2O_2CO_3$ nanosheets at different scan rates in the potential range of −0.1 to 0.4 V *vs.* Ag/AgCl in an aqueous solution of 1 M Na_2SO_4 as an electrolyte. The galvanostatic charge–discharge cycling test (d) and specific capacitances for a number of cycles (e) of $Bi_2O_2CO_3$ nanosheets at the current density 0.1 mA cm^{-2}. EIS plot (f) for different morphologies of $Bi_2O_2CO_3$ at the high frequency region (inset shows the low frequency region).

This journal is © the Owner Societies 2016

Phys. Chem. Chem. Phys., 2016, **18**, 7768–7779 | 7777

reversibility could be promising candidates as electrode materials in electrochemical supercapacitors as well as sensors and batteries.

Conclusions

In summary, $Bi_2O_2CO_3$ with diverse morphologies was successfully synthesized using a simple controllable method. As-synthesized samples demonstrate a tetragonal structure with the well crystalline nature of $Bi_2O_2CO_3$. It was observed that typical reaction parameters and reaction time provide a key factor for control over the morphologies of $Bi_2O_2CO_3$ nanosheets, nanodiscs and nanoplatelets. The N_2 adsorption and ζ-potential measurements of the as-synthesized samples having surface areas 30, 16 and 11 mg g^{-1} (nanosheets, nanodiscs and nanoplatelets) with negative surface charge reveal the efficient adsorption of various dyes (selectively anionic dye) in aqueous solutions. Among them, $Bi_2O_2CO_3$ nanosheets have excellent adsorption capacities of 139.8 and 117.8 mg g^{-1} for acid orange 7 and methyl orange dyes, respectively. Besides, these samples exhibit remarkable photocatalytic activity for the decolorization of cationic dyes (rhodamine B and methyleneblue) from the aqueous solution simulated solar illumination. Furthermore, the $Bi_2O_2CO_3$ nanosheet sample shows a prominent specific electrochemical capacitance of 150 F g^{-1} after 400 cycles for supercapacitor applications. Thus, as-synthesized $Bi_2O_2CO_3$ nanosheets can be excellent materials as adsorbents and photocatalysts for wastewater treatment with supercapacitor activities for energy applications.

Acknowledgements

Notes and references

1 I. Ali, *Chem. Rev.*, 2012, **112**, 5073–5091.
2 X. Chen, L. Liu, P. Y. Yu and S. S. Mao, *Science*, 2011, **331**, 746–750.
3 H. Tong, S. Ouyang, Y. Bi, N. Umezawa, M. Oshikiri and J. Ye, *Adv. Mater.*, 2012, **24**, 229–251.
4 X. Qu, J. Brame, Q. Li and P. J. J. Alvarez, *Acc. Chem. Res.*, 2013, **46**, 834–843.
5 Q. Wu, X. Yang, J. Liu, X. Nie, Y. Huang, Y. Wen, J. Khan, W. U. Khan, M. Wu and T. An, *ACS Appl. Mater. Interfaces*, 2014, **6**, 17730–17739.
6 F. Tian, J. Xiong, H. Zhao, Y. Liu, S. Xiao and R. Chen, *CrystEngComm*, 2014, **16**, 4298–4305.
7 Z. Zhu, Y.-L. Bai, L. Zhang, D. Sun, J. Fang and S. Zhu, *Chem. Commun.*, 2014, **50**, 14674–14677.
8 Y.-C. He, J. Yang, W.-Q. Kan, H.-M. Zhang, Y.-Y. Liu and J.-F. Ma, *J. Mater. Chem. A*, 2015, **4**, 1675–1681.
9 S. Wang, F. Teng and Y. Zhao, *RSC Adv.*, 2015, **5**, 76588–76598.
10 N. M. Tomić, Z. D. Dohčević-Mitrović, N. M. Paunivić, D. Ž. Mijin, N. D. Radić, B. V. Grbić, S. M. Aškrabic, B. M. Babić and D. V. Bajuk-Bogdanović, *Langmuir*, 2014, **30**, 11582–11590.
11 A. Mills, M. Sheik, C. O'Rourke and M. McFarlane, *Appl. Catal., B*, 2009, **89**, 189–195.
12 P. Ji, J. Zhang, F. Chen and M. Anpo, *Appl. Catal., B*, 2009, **85**, 148–154.
13 S. Liang, R. Liang, L. Wen, R. Yuan, L. Wu and X. Fu, *Appl. Catal., B*, 2012, **125**, 103–110.
14 M. Lazar and W. A. Daoud, *RSC Adv.*, 2012, **2**, 447–452.
15 C. Li, M. Wei, D. G. Evans and X. Duan, *Small*, 2014, **10**, 4469–4486.
16 F. Liu, Y. H. Leung, A. B. Djurišić, A. M. C. Ng and W. K. Chan, *J. Phys. Chem. C*, 2013, **117**, 12218–12228.
17 K. Ren, K. Zhang, J. Liu, H. Luo, Y. Huang and X. Yu, *CrystEngComm*, 2012, **14**, 4384–4390.
18 X. Xiao, C. Liu, R. Hu, X. Zuo, J. Nan, L. Li and L. Wang, *J. Mater. Chem.*, 2012, **22**, 22840–22843.
19 F. Qin, G. Li, H. Xiao, Z. Lu, H. Sun and R. Chen, *Dalton Trans.*, 2012, **41**, 11263–11266.
20 C. F. Guo, J. Zhang and Q. Liu, *ACS Nano*, 2012, **6**, 8746–8752.
21 Q.-C. Liu, D.-K. Ma, Y.-Y. Hu, Y.-W. Zeng and S.-M. Huang, *ACS Appl. Mater. Interfaces*, 2013, **5**, 11927–11934.
22 Y. Huang, H. Li, M.-S. Balogun, W. Liu, Y. Tong, X. Lu and H. Ji, *ACS Appl. Mater. Interfaces*, 2014, **6**, 22920–22927.
23 M. Roy, S. Ghosh and M. K. Naskar, *Phys. Chem. Chem. Phys.*, 2015, **17**, 10160–10169.
24 F. Wang, Z. Zhao, K. Zhang, F. Dong and Y. Zhou, *CrystEngComm*, 2015, **17**, 6098–6102.
25 S. Sun and W. Wang, *RSC Adv.*, 2014, **4**, 47136–47512.
26 F. Qin, G. Li, R. Wang, J. Wu, H. Su and R. Chen, *Chem. – Eur. J.*, 2012, **18**, 16491–16497.
27 J. Li, Y. Yu and L. Zhang, *Nanoscale*, 2014, **6**, 8473–8488.
28 R. Chen, M. H. So, J. Yang, F. Deng, C.-M. Che and H. Sun, *Chem. Commun.*, 2006, 2265–2267.
29 Y. Zheng, F. Duan, M. Chen and Y. Xie, *J. Mol. Catal. A: Chem.*, 2010, **317**, 34–40.
30 F. Dong, W.-K. Ho, S. C. Lee, Z. Wu, M. Fu, S. Zou and Y. Huang, *J. Mater. Chem.*, 2011, **21**, 12428–12436.
31 P. Madhusudan, J. Zhang, B. Cheng and G. Liu, *CrystEngComm*, 2013, **15**, 231–240.
32 T. Selvamani, A. M. Asiri, A. O. Al-Youbi and S. Anandan, *Mater. Sci. Forum*, 2013, **764**, 169–193.
33 T. Xiong, F. Dong and Z. Wu, *RSC Adv.*, 2014, **4**, 56307–56312.
34 Z. Zhao, Y. Zhou, F. Wang, K. Zhang, S. Yu and K. Cao, *ACS Appl. Mater. Interfaces*, 2015, **7**, 730–737.
35 H. Huang, J. Wang, F. Dong, Y. Guo, N. Tian, Y. Zhang and T. Zhang, *Cryst. Growth Des.*, 2015, **15**, 534–537.
36 Y. Zhou, H. Wang, M. Sheng, Q. Zhang, Z. Zhao, Y. Lin, H. Liu and G. R. Patzke, *Sens. Actuators, B*, 2013, **188**, 1312–1318.

7778 | *Phys. Chem. Chem. Phys.*, 2016, **18**, 7768–7779

This journal is © the Owner Societies 2016

37 S. Peng, L. Li, H. Tan, Y. Wu, R. Cai, H. Yu, X. Huang, P. Zhu, S. Ramakrishna, M. Srinivasan and Q. Yan, *J. Mater. Chem. A*, 2013, **1**, 7630–7638.

38 D. Barreca, F. Morazzoni, G. A. Rizzi, R. Scotti and E. Tondello, *Phys. Chem. Chem. Phys.*, 2001, **3**, 1743–1749.

39 X. Zhang, Y. Zheng, D. G. McCulloch, L. Y. Yeo, J. R. Friend and D. R. MacFarlane, *J. Mater. Chem. A*, 2014, **2**, 2275–2282.

40 H.-Y. Jiang, P. Li, G. Liu, J. Ye and J. Lin, *J. Mater. Chem. A*, 2015, **3**, 5119–5125.

41 J. Eberl and H. Kisch, *Photochem. Photobiol. Sci.*, 2008, **7**, 1400–1406.

42 P. Taylor, S. Sunder and V. J. Lopata, *Can. J. Chem.*, 1984, **62**, 2863–2873.

43 H. Cheng, B. Huang, K. Yang, Z. Wang, X. Qin, X. Zhang and Y. Dai, *ChemPhysChem*, 2010, **11**, 2167–2173.

44 L. Chen, R. Huang, S.-F. Yin, S.-L. Luo and C.-T. Au, *Chem. Eng. J.*, 2012, **193–194**, 123–130.

45 F. Dong, S. C. Lee, Z. Wu, Y. Huang, M. Fu, W.-K. Ho, S. Zou and B. Wang, *J. Hazard. Mater.*, 2011, **195**, 346–354.

46 F. Dong, Y. Sun, M. Fu, W.-K. Ho, S. C. Lee and Z. Wu, *Langmuir*, 2012, **28**, 766–773.

47 F. Dong, A. Zheng, Y. Sun, M. Fu, B. Jiang, W.-K. Ho, S. C. Lee and Z. Wu, *CrystEngComm*, 2012, **14**, 3534–3544.

48 F. Dong, Y. Sun, W.-K. Ho and Z. Wu, *Dalton Trans.*, 2012, **41**, 8270–8284.

49 F. Dong, J. Bian, Y. Sun, T. Xiong and W. Zhang, *CrystEngComm*, 2014, **16**, 3592–3604.

50 Y. Liu, Z. Wang, B. Huang, K. Yang, X. Zhang, X. Qin and Y. Dai, *Appl. Surf. Sci.*, 2010, **257**, 172–175.

51 R. Chen, G. Cheng, M. H. So, J. Wu, Z. Lu, C.-M. Che and H. Sun, *Mater. Res. Bull.*, 2010, **45**, 654–658.

52 X.-F. Cao, L. Zhang, X.-T. Chen and Z.-L. Xue, *CrystEngComm*, 2011, **13**, 1939–1945.

53 T. Zhao, J. Zai, M. Xu, Q. Zou, Y. Su, K. Wang and X. Qian, *CrystEngComm*, 2011, **13**, 4010–4017.

54 F. Dong, Q. Li, W. Zhang, M. Guan, W.-K. Ho and Z. Wu, *Mater. Chem. Phys.*, 2013, **142**, 381–386.

55 L. Yang, Q. Han, J. Zhu and X. Wang, *Mater. Lett.*, 2015, **138**, 235–237.

56 G. Cheng, J. Wu, F. Xiao, H. Yu, Z. Lu, X. Yu and R. Chen, *Mater. Lett.*, 2009, **63**, 2239–2242.

57 G. Cheng, H. Yang, K. Rong, Z. Lu, X. Yu and R. Chen, *J. Solid State Chem.*, 2010, **183**, 1878–1883.

58 H. Y. Liang, Y. X. Yang, J. C. Tang and M. Ge, *Mater. Sci. Semicond. Process.*, 2013, **16**, 1650–1654.

59 F. Dong, T. Xiong, Y. Sun, H. Huang and Z. Wu, *J. Mater. Chem. A*, 2015, **3**, 18466–18474.

60 J. Tang, H. Zhao, G. Li, Z. Lu, S. Xiao and R. Chen, *Ind. Eng. Chem. Res.*, 2013, **52**, 12604–12612.

61 S. Liu, Y. Tu and G. Dai, *Ceram. Int.*, 2014, **40**, 2343–2348.

62 W. Cen, T. Xiong, C. Tang, S. Yuan and F. Dong, *Ind. Eng. Chem. Res.*, 2014, **53**, 15002–15011.

63 F. Dong, H. Liu, W.-K. Ho, M. Fu and Z. Wu, *Chem. Eng. J.*, 2013, **214**, 198–207.

64 C.-M. Lan, S.-E. Liu, J.-W. Shiu, J.-Y. Hu, M.-H. Lin and E. W.-G. Diau, *RSC Adv.*, 2013, **3**, 559–565.

65 T. Selvamani, T. Yagyu, S. Kawasaki and I. Mukhopadhyay, *Catal. Commun.*, 2010, **11**, 537–541.

66 T. Selvamani, C. A. Manjula, S. Anandan, A. M. Asiri and M. Ashokkumar, *Cryst. Res. Technol.*, 2015, **50**, 143–149.

67 H. Huang, K. Xiao, S. Yu, F. Dong, T. Zhang and Y. Zhang, *Chem. Commun.*, 2016, **52**, 354–357.

68 L. Shan, G. Wang, D. Li, X. San, L. Liu, L. Dong and Z. Wu, *Dalton Trans.*, 2015, **44**, 7835–7843.

69 H. Huang, X. Li, J. Wang, F. Dong, P. K. Chu, T. Zhang and Y. Zhang, *ACS Catal.*, 2015, **5**, 4094–4103.

70 G. E. Tobon-Zapata, S. B. Etcheverry and E. J. Baran, *J. Mater. Sci. Lett.*, 1997, **16**, 656–657.

71 X. Xiao, R. Hu, C. Liu, C. Xing, C. Qian, X. Zuo, J. Nan and L. Wang, *Appl. Catal., B*, 2013, **140–141**, 433–443.

72 K. S. W. Sing, D. H. Everett, R. A. W. Haul, L. Moscou, R. A. Pierotti, J. Rouquérol and T. Siemieniewska, *Pure Appl. Chem.*, 1985, **57**, 603–619.

73 K. Kaneko, *J. Membr. Sci.*, 1994, **96**, 59–89.

74 C. Pan, J. Xu, Y. Chen and Y. Zhu, *Appl. Catal., B*, 2012, **115–116**, 314–317.

75 S. Obregón and G. Colón, *J. Mol. Catal. A: Chem.*, 2013, **376**, 40–47.

76 Y. Lei, G. Wang, S. Song, W. Fan, M. Pang, J. Tang and H. Zhang, *Dalton Trans.*, 2010, **39**, 3273–3278.

77 S. Anandan, G.-L. Lee, P.- K. Chen, C. Fan and J. J. Wu, *Ind. Eng. Chem. Res.*, 2010, **49**, 9729–9737.

78 N. Liang, J. Zai, M. Xu, Q. Zhu, X. Wei and X. Qian, *J. Mater. Chem. A*, 2014, **2**, 4208–4216.

79 D.-H. Wang, G.-Q. Gao, Y.-W. Zhang, L.-S. Zhou, A.-W. Xu and W. Chen, *Nanoscale*, 2012, **4**, 7780–7785.

80 M. Xiong, L. Chen, Q. Yuan, J. He, S.-L. Luo, C.-T. Au and S.-F. Yin, *Dalton Trans.*, 2014, **43**, 8331–8337.

81 J. Tang, D. Li, Z. Feng, Z. Tan and B. Ou, *RSC Adv.*, 2014, **4**, 2151–2154.

82 B. G. S. Raj, R. N. R. Ramprasad, A. M. Asiri, J. J. Wu and S. Anandan, *Electrochim. Acta*, 2015, **156**, 127–137.

83 D. Wang, Q. Wang and T. Wang, *Nanotechnology*, 2011, **22**, 135604.

84 M. Toupin, T. Brousse and D. Bélanger, *Chem. Mater.*, 2002, **14**, 3946–3952.

85 W. Sugimoto, H. Iwata, Y. Yasunaga, Y. Murakami and Y. Takasu, *Angew. Chem.*, 2003, **115**, 4226–4230.

86 Y. Liu, W. Wang, Y. Wang, Y. Ying, L. Sun and X. Peng, *RSC Adv.*, 2014, **4**, 16374–16379.

This journal is © the Owner Societies 2016

Phys. Chem. Chem. Phys., 2016, **18**, 7768–7779 | 7779